SOFT ROBOTS

Heterogeneous sensing in a multifunctional soft sensor for human-robot interfaces

Taekyoung Kim[1,2,3], Sudong Lee[1,2,3], Taehwa Hong[1,2,3], Gyowook Shin[1,2,3], Taehwan Kim[1,2,3], Yong-Lae Park[1,2,3]*

Soft sensors have been playing a crucial role in detecting different types of physical stimuli to part or the entire body of a robot, analogous to mechanoreceptors or proprioceptors in biology. Most of the currently available soft sensors with compact form factors can detect only a single deformation mode at a time due to the limitation in combining multiple sensing mechanisms in a limited space. However, realizing multiple modalities in a soft sensor without increasing its original form factor is beneficial, because even a single input stimulus to a robot may induce a combination of multiple modes of deformation. Here, we report a multifunctional soft sensor capable of decoupling combined deformation modes of stretching, bending, and compression, as well as detecting individual deformation modes, in a compact form factor. The key enabling design feature of the proposed sensor is a combination of heterogeneous sensing mechanisms: optical, microfluidic, and piezoresistive sensing. We characterize the performance on both detection and decoupling of deformation modes, by implementing both a simple algorithm of threshold evaluation and a machine learning technique based on an artificial neural network. The proposed soft sensor is able to estimate eight different deformation modes with accuracies higher than 95%. We lastly demonstrate the potential of the proposed sensor as a method of human-robot interfaces with several application examples highlighting its multifunctionality.

INTRODUCTION

Soft robotics has been studied to increase the adaptability of robots to their surroundings and to humans (*1*–*10*) for more efficient and safer collaboration and interaction. To improve the adaptability of robots, soft sensors have been actively developed by implementing different sensing mechanisms, such as the detection of electrical properties [e.g., resistance (*11*–*16*) and capacitance (*17*–*22*)] or optical properties [e.g., light intensity (*23*–*28*) and wavelength (*29*–*32*)]. These soft sensors can be fabricated by combining different types of materials, including liquid [e.g., ionic liquids (*33*–*39*) and liquid metals (*40*–*44*)], nanomaterials [e.g., carbon nanotubes (*45*–*49*) and gold or silver nanowires (*50*–*55*)], conductive fabrics (*21*, *56*–*59*), and optical or optoelectronic materials [e.g., photodiodes, light-emitting diodes (LEDs), and waveguides (*23*–*28*)]. They can play a crucial role in detecting different types of physical stimuli to part or the entire body of a robot, analogous to mechanoreceptors or proprioceptors in biology.

However, most currently available soft sensors are based on a single sensing mechanism that can detect only one deformation mode at a time, although it can be responsive to more than one mode, such as compression, stretching, and bending. Microfluidic soft sensors change the electrical resistances of liquid-filled microchannels encapsulated by an elastomer matrix when compressed or stretched (*11*–*16*, *60*–*63*). Soft optical waveguides cause an optical power loss in transmission when stretched or bent (*25*–*28*, *64*, *65*). Conductive fabric sensors change the capacitance between the two layers when stretched or compressed (*21*, *56*–*59*). Although all of the sensors can be responsive to multiple types of physical deformation, they cannot distinguish the types of deformation with only a single sensing element.

In real-world robotics applications, because a single input stimulus to a robot may induce a combination of multiple modes of deformation, realizing additional modalities in a soft sensor without increasing its structural complexity or the form factor (the basic size necessary to realize the original sensing mode) is useful to understand and control the response behaviors of the robot. There have been efforts to develop soft sensing structures with multimodalities for detecting different deformation modes simultaneously (*66*, *67*). Multiple modalities in soft sensors can be enabled by various approaches. Examples include a multilayered elastomer structure embedded with conductive fluidic channels (*11*, *68*, *69*) and multiple identical (*70*, *71*) or heterogeneous (*72*, *73*) sensing elements closely packaged in an elastomer structure. Details on the state of the art on multimodal sensing can be found in note S1. To have a multimodal sensing capability (i.e., the capability of detecting or decoupling different types of stimuli applied to the sensor at the same time) in the above structures, multiple sensing elements, whether they share the same mechanism, need to be physically combined together to form one sensing structure. This may cause the design and the fabrication process to be complex or may increase the size of the structure, as shown in the multilayered soft skin sensor with embedded microfluidic channels (*11*) or the multimodal sensor fabricated of multilayered copper-polyimide film electrodes (*70*).

To overcome these limitations, we propose a multifunctional soft sensor capable of detecting single-mode deformation—such as stretching, bending, or compression, individually—and decoupling those combined modes simultaneously (Movie 1). This multifunctionality is possible because three heterogeneous sensing mechanisms—optoelectronics, microfluidics, and piezoresistivity—are packaged in a single compact sensor. The heterogeneity of the three mechanisms enables physical sharing of the primary sensing structure without interfering with each other, simplifying the design and fabrication

[1]Department of Mechanical Engineering, Seoul National University, Seoul 08826, Korea. [2]Institute of Advanced Machines and Design (IAMD), Seoul National University, Seoul 08826, Korea. [3]Institute of Engineering Research, Seoul National University, Seoul 08826, Korea.
*Corresponding author. Email: ylpark@snu.ac.kr

of the sensor, and providing a compact form factor. The sensor structure can be divided into three parts: a microfluidic channel filled with ionic liquid, an elastomer housing, and an outside conductive fabric layer. The ionic liquid channel is used as a microfluidic sensor that changes its electrical resistance with deformation while it becomes the core of an optical waveguide at the same time due to the optical transparency of the liquid. The elastomer housing then works as the cladding for the waveguide with a different refractive index from that of the ionic liquid, enabling total internal reflection while providing the soft structure for the conductive fabrics to be attached. Because these multiple sensing elements yield different output patterns depending on the types of input deformation, our sensor is able to detect both single-mode deformations and combined deformation modes through analysis of the output patterns. In this work, two different analysis methods were used: threshold evaluation and machine learning. The threshold evaluation algorithm simply presets the threshold value of each sensor signal and rejects the sensor output if it is below the threshold (*74*, *75*). It is simple and relatively powerful to determine the single-mode deformation. However, it is not straightforward whether the deformation is combined with two or more modes. To address this issue, we used a machine learning technique based on an artificial neural network (ANN) (*76*, *77*) for detecting and decoupling multimode deformations. Consequently, the multifunctionality of the proposed sensor is suitable as a method for human-robot interfaces and for mechanoreception and/or proprioception of soft robots, considering its structural simplicity and compactness.

The rest of the paper is organized as follows. First, we describe the design of the sensing structure composed of three sensing elements—such as the soft optical waveguide, the ionic liquid channel, and the conductive fabric layer—densely packaged in an elastomer body. Second, we discuss the working mechanisms of the three sensing elements on physical deformations with simulation results. For the results, we experimentally characterize a single sensor with different input modes. Third, we evaluate the performance of mode classification with a simple threshold evaluation method and with an ANN-based machine learning technique. In addition, we demonstrate the potential applications of the proposed sensor as a method of human-robot interfaces, highlighting its multifunctionality. Last, we conclude with a discussion and future work.

RESULTS

Design of sensing structure

The design of the proposed sensor uses heterogeneous sensing mechanisms that detect changes of light intensity and electrical resistance with three different sensing elements, packaged in a single soft sensor, as shown in Fig. 1A: an optical waveguide integrated with a LED and a photodiode, a microfluidic channel filled with a room-temperature ionic liquid (RTIL), and a conductive fabric layer. To integrate all of the elements in a single sensor, a cylindrical fluidic channel filled with RTIL is first located at the center of the sensor, aligned to the neutral axis. A soft silicone housing encapsulates this channel, and the two ends of the channel are equipped with an LED and a photodiode, respectively (Fig. 1A, top). The liquid-filled channel works as a waveguide, a passage through which the light from the LED propagates toward the photodiode, and changes its electrical resistance when deformed. On the surface of the waveguide, the conductive fabric is attached to all four sides of the housing, which are electrically connected in parallel to each other (Fig. 1A, top). Last, the waveguide and the conductive fabric layer are coated with a black nontransparent silicone layer for preventing optical disturbances from the ambient light and for physically protecting the conductive fabric layer and the waveguide (Fig. 1A, bottom). The entire structure of the final prototype has a square cross section with each side of 10 mm and a length of 70 mm. The core of the waveguide has a circular cross section with a diameter of 2.5 mm and a length of 66 mm, which is the same as the length of its cladding. The cladding has a square cross section with the length of each side of 6 mm. Figure 1 (B to D) shows the actual prototype of the proposed sensor.

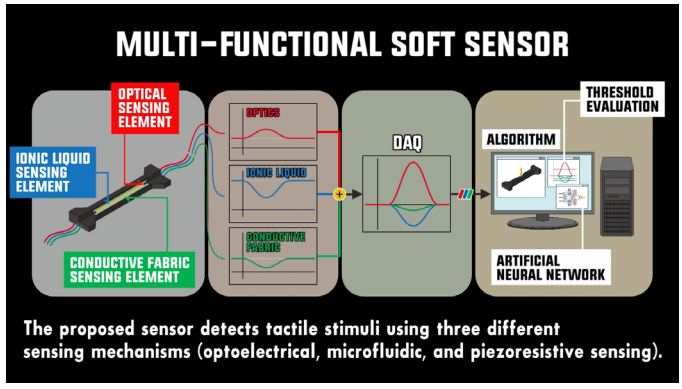

Movie 1. Summary of heterogeneous sensing mechanisms for a soft multifunctional sensor.

Heterogeneous sensing mechanisms

Soft optical waveguide

One of the most common mechanisms of optical waveguides is the total internal reflection, enabled by the difference of the refractive indices of the core and the cladding materials, which has been typically used in fiber optics. The total internal reflection occurs when the input angle of the light from the source to the boundary of the core is larger than the critical angle. As long as the refractive index of the cladding is smaller than that of the core, the light emitted from the LED can propagate to the photodiode through the core by total internal reflection. Then, the light intensity can be measured by the photodiode. When the sensor is physically deformed, however, the amount of the transmitted light is reduced because of the frustration in total internal reflection, resulting in optical power loss. Consequently, we can detect the changes of the voltage drop in the photodiode.

In our design, the medium materials of the core and the cladding are RTIL and elastomer, respectively. The refractive index of the RTIL (1-ethyl-3-methylimidazolium ethyl sulfate, Alfa Aesar) (n = 1.48) is larger than that of the silicone elastomer (SORTA-Clear 12, Smooth-On) (n = 1.41) for the cladding, which is enough to create the total internal reflection, as shown in Fig. 1E (i). The low attenuation rate of the RTIL due to the optical transparency also facilitates optical transmission. Because any type of physical deformation can cause enough frustration in optical transmission of the waveguide, the optical signals are sensitive to all three deformation modes of stretching, bending, and compression.

Ionic liquid channel

The waveguide core can also be used as a microfluidic channel for detecting physical deformation, such as strain or compression, because the RTIL is electrically conductive. The liquid channel changes its electrical resistance based on the geometrical changes in length or

cross-sectional area when stretched or locally compressed, respectively, as illustrated in Fig. 1E (ii). However, pure bending does not change the channel's length, and the resistance will consequently remain the same during bending because the liquid channel is located along the neutral axis. Therefore, the RTIL channel is sensitive to stretching and compression only.

Conductive fabric layer

The conductive fabric used in our sensor is a silver-plated knitted fabric, fabricated by weaving silver (Ag)–coated nylon fibers with a pattern in a particular direction (Fig. 1E, iii, and see fig. S1, i). The conductivity of the fabric is affected by the amount of contacts between the nylon fibers. The stretching direction also affects the conductivity depending on the shape of the pattern of the fibers. The fabric layer is laminated on the surface of the elastomer cladding of the waveguide along the length in our sensor. A decrease in angles between fibers also causes larger contact areas in the fibers. As a result, the overall electrical resistance of the fabric layer decreases when stretched. The resistance of the fabric layer decreased by 52% from the initial state when it was stretched to 50% (see fig. S1, ii). However, the contact angles of the fibers decrease only in a small area when the fabric was locally compressed, resulting in a slight change in the overall resistance. The resistance of the fabric layer decreased by only 6.1% from the initial state when a local pressure of 110 kPa was applied to an area of 50.27 mm^2 (see fig. S1, iii). This change is not negligible but small enough to be rejected in our algorithms of mode classification. When the sensor is bent, only one of the four sides of the fabric layer shows a slight decrease in its resistance due to compressive stress, resulting in a negligible change in the overall resistance. Therefore, the conductive fabric layer is only sensitive when the sensor is stretched.

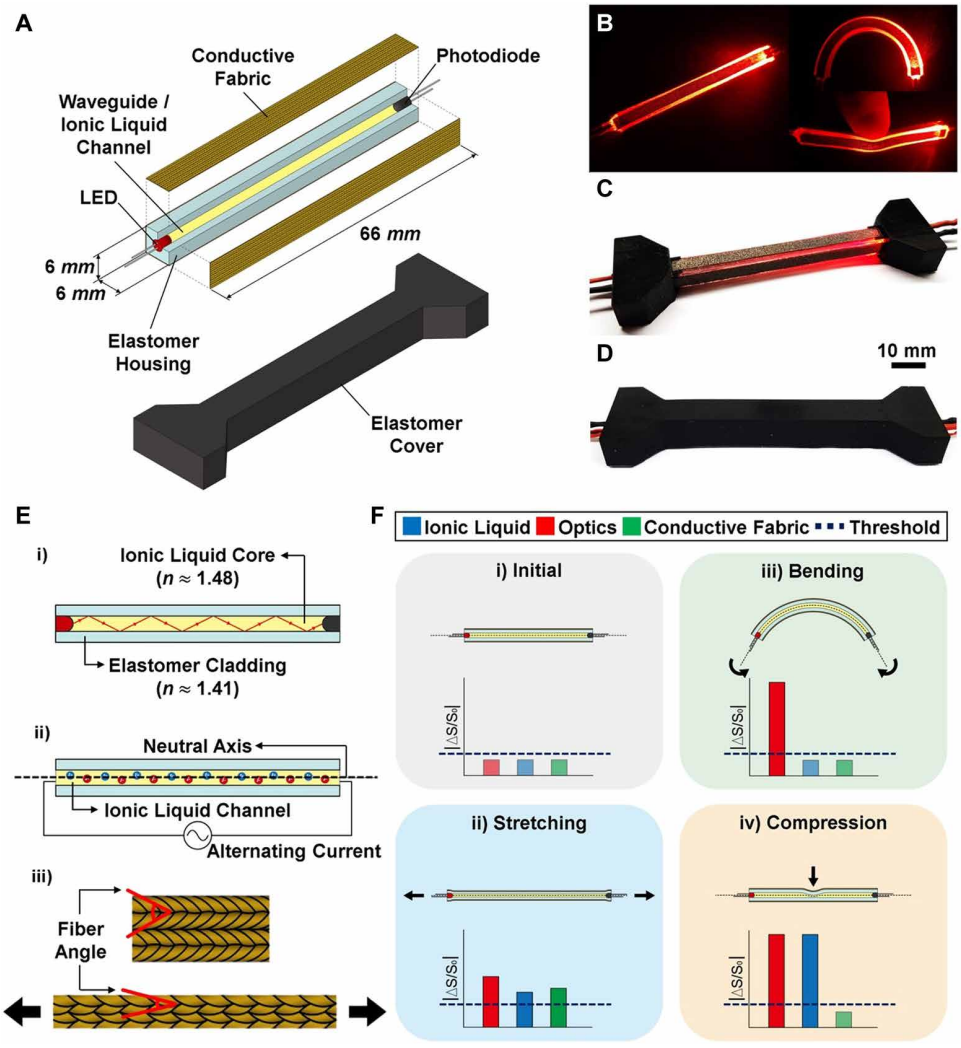

Fig. 1. Design and sensing mechanisms of the proposed multifunctional soft sensor. (**A**) Soft sensor design with key components for three different sensing elements. (**B**) Soft optical waveguide composed of elastomer cladding and liquid core of RTIL. (**C**) Conductive fabric layer laminated to the waveguide. (**D**) Final prototype of the proposed soft sensor. (**E**) Working principles of three sensing elements: (i) optical sensing by total internal reflection of soft waveguide (*n*, refractive index), (ii) principle of RTIL sensing based on the movements of ions, and (iii) principle of conductive fabric sensing based on the angle of the fibers. (**F**) Output signal pattern for different deformation modes: (i) initial (no deformation), (ii) stretching, (iii) bending, and (iv) compression. The magnitudes of the bars are qualitative representations of different signal patterns for different input deformation modes.

Simulation of three sensing mechanisms

We conducted simulations on mechanical, electrical, and optical responses to three deformation modes of stretching, bending, and compression, using a commercial finite element analysis (FEA) software package (COMSOL Multiphysics) to verify the mechanisms of the proposed sensor before fabrication (see fig. S2 and movie S1). According to the simulation results, the change in light intensity was sensitive to all three deformation modes (see fig. S2A, i to iii). The RTIL channel was responsive to both stretching and compression but not to bending (see fig. S2B, i to iii). The conductive fabric layer showed sensitivity only to stretching (see fig. S2C, i to iii). These distinctive output patterns depending on the deformation types, therefore, verify the feasibility of decoupling multiple deformation modes, as shown in Fig. 1F (i to iv).

Sensor characterization

Single-mode deformation test

The sensor prototype was individually characterized with three different deformation modes: (i) stretching, (ii) bending, and (iii) local compression (see fig. S3 and movie S2 for the single-mode deformation tests). The output signals were normalized (dV/V_0, df/f_0, and dV/V_0 for stretching, bending, and compression, respectively) so that the sensitivities to different deformations can be easily compared.

The sensor was first stretched up to 50% (33 mm) from its original length (66 mm), as shown in fig. S3 (i). Figure 2A shows the sensor data of 10 test cycles. Among the three sensing elements in the prototype, the optical sensing showed the highest output of +1.04 (dV/V_0) at the

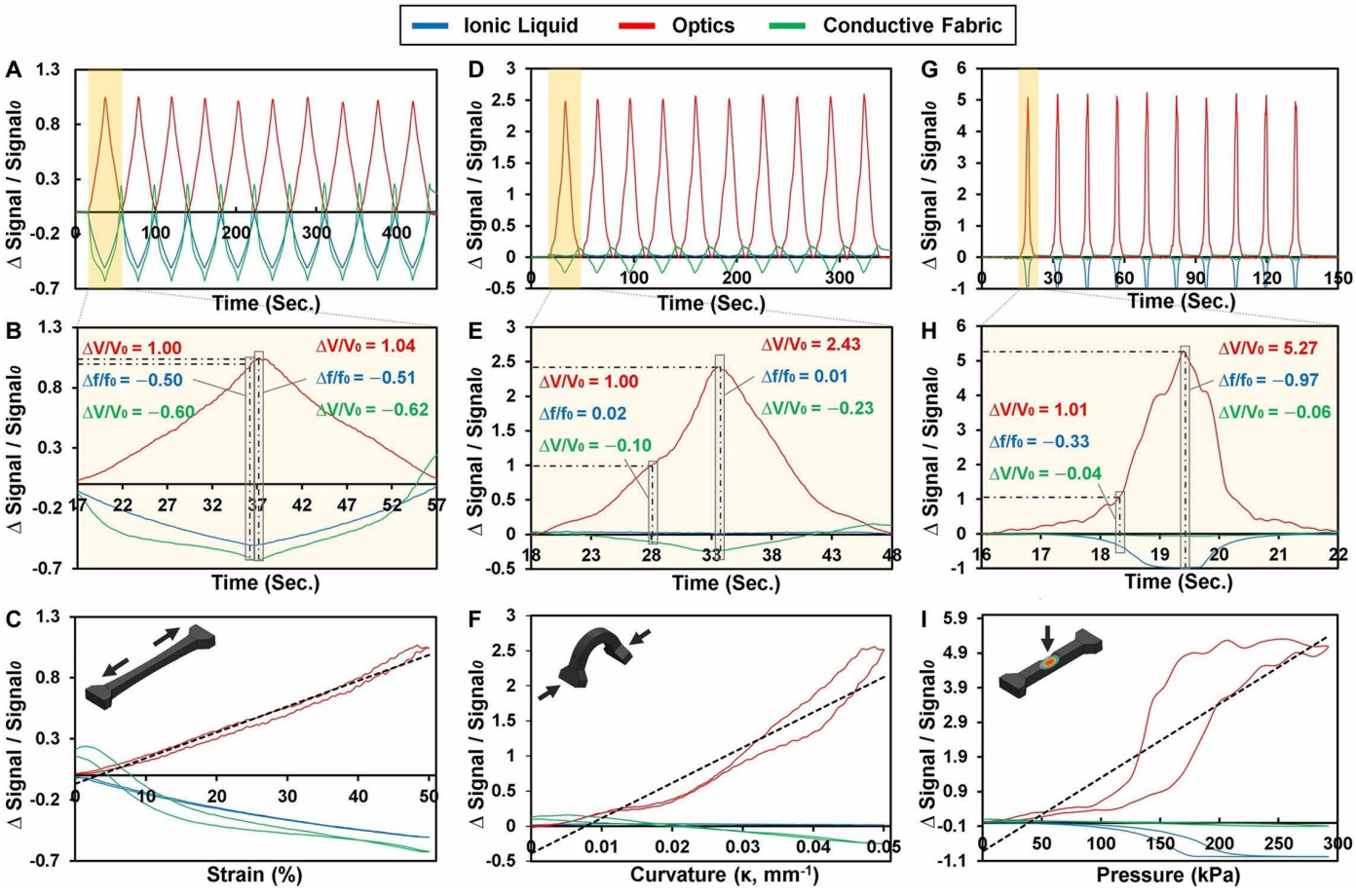

Fig. 2. Characterization results of the proposed soft sensor for single-mode deformations. (**A**) Tensile test result of loading-unloading loops for 10 cycles. (**B**) Close-up view of a single cycle from the tensile test result. (**C**) Normalized sensor output of the single tensile test cycle versus strain. (**D**) Bending test result of loading-unloading loops for 10 cycles. (**E**) Close-up view of a single cycle from the bending test. (**F**) Normalized sensor output of the single bending test versus curvature. (**G**) Compression test result of loading-unloading loops for 10 cycles. (**H**) Close-up view of a single cycle from the compression test. (**I**) Normalized sensor output of the single compression test versus pressure.

maximum strain of 50% (Fig. 2B). The nonlinearity of the optical sensing was 16.25% (Fig. 2C). The outputs of the RTIL channel (df/f_0) and the conductive fabric (dV/V_0) were −0.51 and −0.62, respectively, at the maximum strain. The outputs from all three sensing elements also showed high repeatability during the cyclic test (see fig. S4A).

For the bending test, the sensor was bent by pushing the two ends using the test setup in fig. S3 (ii). The free-rotation joints of the holders at the two ends enabled the pure bending of the sensor. The displacement of each end was 25 mm toward the center of the sensor. The result for the range of curvature from 0 to 0.05 mm^{-1} with 10 cycles is shown in Fig. 2D. The optical sensing showed the highest output of +2.43 (dV/V_0) with the maximum bending curvature ($\kappa = 0.05\ mm^{-1}$) (Fig. 2E). The nonlinearity of the optical signal was 26.82% (Fig. 2F), which was larger than that from the stretching test. The outputs of the RTIL channel (df/f_0) and the conductive fabric layer (dV/V_0) at the maximum curvature were +0.01 and −0.23, respectively (Fig. 2E). It can be noted that the sensitivity of the RTIL sensing is almost zero, as expected because pure bending hardly changed the resistance of the liquid channel. All three sensor outputs were reliable during the cyclic bending test as well (fig. S4B).

The compression test was conducted using a cylindrical indenter with a flat contact surface (diameter, 10 mm) fabricated by three-dimensional (3D) printing and a commercial load cell (RFT60-HA01, ROBOTOUS), as shown in fig. S3 (iii). The indenter applied a local pressure from 0 to 292 kPa by deforming the middle area of the top surface of the sensor with a displacement of up to 5 mm. The sensor output from 10 cycles of compression is shown in Fig. 2G. The optical sensing showed a high nonlinearity of 36.3% and an exponential loading-unloading loop with hysteresis (Fig. 2I), commonly observed in most microfluidic soft sensors (*78*–*80*). The output from the optical sensing (dV/V_0) was +5.27 at the maximum pressure of 292 kPa (Fig. 2H). The sensitivity of the optical sensing substantially increased. The outputs of the RTIL channel (df/f_0) and the conductive fabric (dV/V_0) were −0.97 and −0.06, respectively. The RTIL signal changed almost up to the saturation level, whereas the output level of the conductive fabric was almost negligible, because a local compression in a small area of the fabric did not contribute to the change of the overall resistance. The sensor outputs were reliable during the cyclic test (fig. S4C).

The normalized output values of the three sensing elements were compared for each deformation mode when the output of the optical sensor was 1. The sensor outputs of the RTIL channel and the conductive fabric were −0.50 and −0.60 for stretching, 0.02 and −0.10 for bending, and −0.33 and −0.04 for compression, respectively.

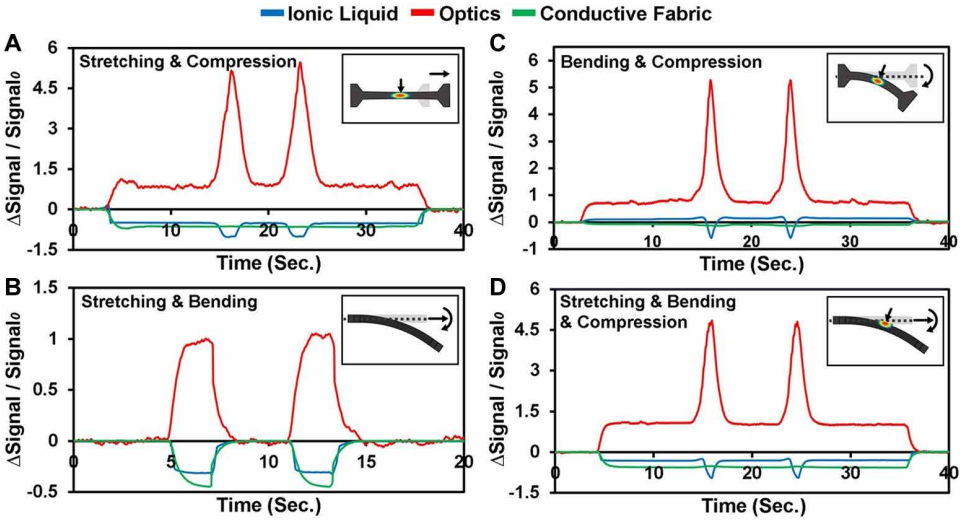

Fig. 3. Characterization results of multifunctional sensing with combined deformation modes. (**A**) Stretching and compression. (**B**) Stretching and bending. (**C**) Bending and compression. (**D**) Stretching, bending, and compression.

The optical sensor was sensitive to all three deformation modes. However, the RTIL channel was sensitive to stretching and compression but not to bending, and the conductive fabric was sensitive to compression only. The characterization results confirm that all three deformation modes can be detected by analyzing the output patterns.

Multimode deformation test

We tested the sensor with multimode inputs as well, as shown in Fig. 3. Each test was conducted by applying two or all three deformation inputs (i.e., stretching, bending, and compression) to the sensor at the same time (see movie S3).

For simultaneous stretching and compression, the sensor was first stretched up to the 50% from its original length, and then a local contact pressure was applied in the middle of the stretched sensor. The stretched state of the sensor created offsets in the output signals of the three sensing elements. When the sensor was locally compressed, the optical and the RTIL sensing signals showed additional changes, whereas the conductive fabric signal remained the same (Fig. 3A).

For simultaneous stretching and bending, the sensor was bent off the neutral axis of a rotational joint. The distance of the sensor from the neutral axis of the joint (20 mm) enabled simultaneous stretching and bending. All three sensing elements showed responses similar to those from the stretching test (Fig. 3B). Although the sensor was stretched only up to 23% in this test, the magnitude of the output signal from the optical sensor was almost as large as that of 50% strain in the single-mode test due to the superposition of two output signals from the two deformation modes.

For simultaneous bending and compression, the sensor was first rotated on the neutral axis of a rotational joint, and then a local contact pressure was applied. Only the optical sensing showed an offset in the output from bending in this test. With compression, the optical and the RTIL sensing signals showed changes, whereas the signal from the conductive fabric remained the same (Fig. 3C).

To apply combined inputs of all three deformations, the sensor was first bent off the neutral axis of a rotational joint, and then a local contact pressure was applied. All three sensing signals showed offsets in the output with the combined input of stretching and bending. When an input of compression was added, the optical and the RTIL signals showed additional changes, whereas the conductive fabric signal remained the same (Fig. 3D).

Calibration of optical sensor signal

Because the optical signal was responsive to all three deformation modes and more sensitive than the other two signals, it was used to estimate the magnitude of each deformation mode. An experiment was conducted to calibrate the magnitudes of the three deformations with the optical signals (fig. S5). The mean values with the SD bars of five trials for each deformation are provided in fig. S5, and the sensor characteristics (linearity, accuracy, and sensitivity) are summarized in table S1.

Effect of localized deformation

In the case of bending or compression in which the deformation is concentrated on a local area, the location of the deformation can affect the output sensitivity of the sensor signal. Additional bending and compression tests were conducted to characterize the influence of deformation locations on the output signals. Bending and compression were separately applied at the center of the sensor and at a location 15 mm away from the center (see fig. S6). In this experiment, the curvature was applied up to 0.04 mm^{-1}, and the pressure was applied up to 230 kPa. In both bending and compression, the magnitude of the optical signal was larger when the deformation location was close to the end of the sensor than when it was at the center. However, the output signals did not show substantial differences in the cases of the ionic liquid and the conductive fabric (see fig. S7). Although the sensitivity of the optical signals changed depending on the locations, the general output patterns of the three sensing elements were not affected by the deformation locations.

Temperature sensitivity

The conductivity of an ionic liquid varies depending on its temperature (*81*–*84*). Experiments were conducted to confirm the influence of temperature on the output of the ionic liquid sensor. The results confirmed that temperature compensation may be necessary when the ambient temperature is higher than 40°C (see note S2 and figs. S8 and S9).

Classification of deformation modes

Single-mode deformation

We tested two different algorithms, based on a simple threshold evaluation and on machine learning with an ANN, for detecting each deformation mode. (Details on the process of these methods are described in Materials and Methods, Fig. 4A, and figs. S10 and S11.)

Figure 4B shows the sensing signals obtained by stretching, bending, or compressing the sensor prototype and the estimated deformation states through the threshold evaluation algorithm (see movie S4). The algorithm found correct deformation states most of the time during the test. However, it sometimes showed errors for a short period at the boundaries of the events. For example, there is a delay in estimating the state, although the optical sensing already

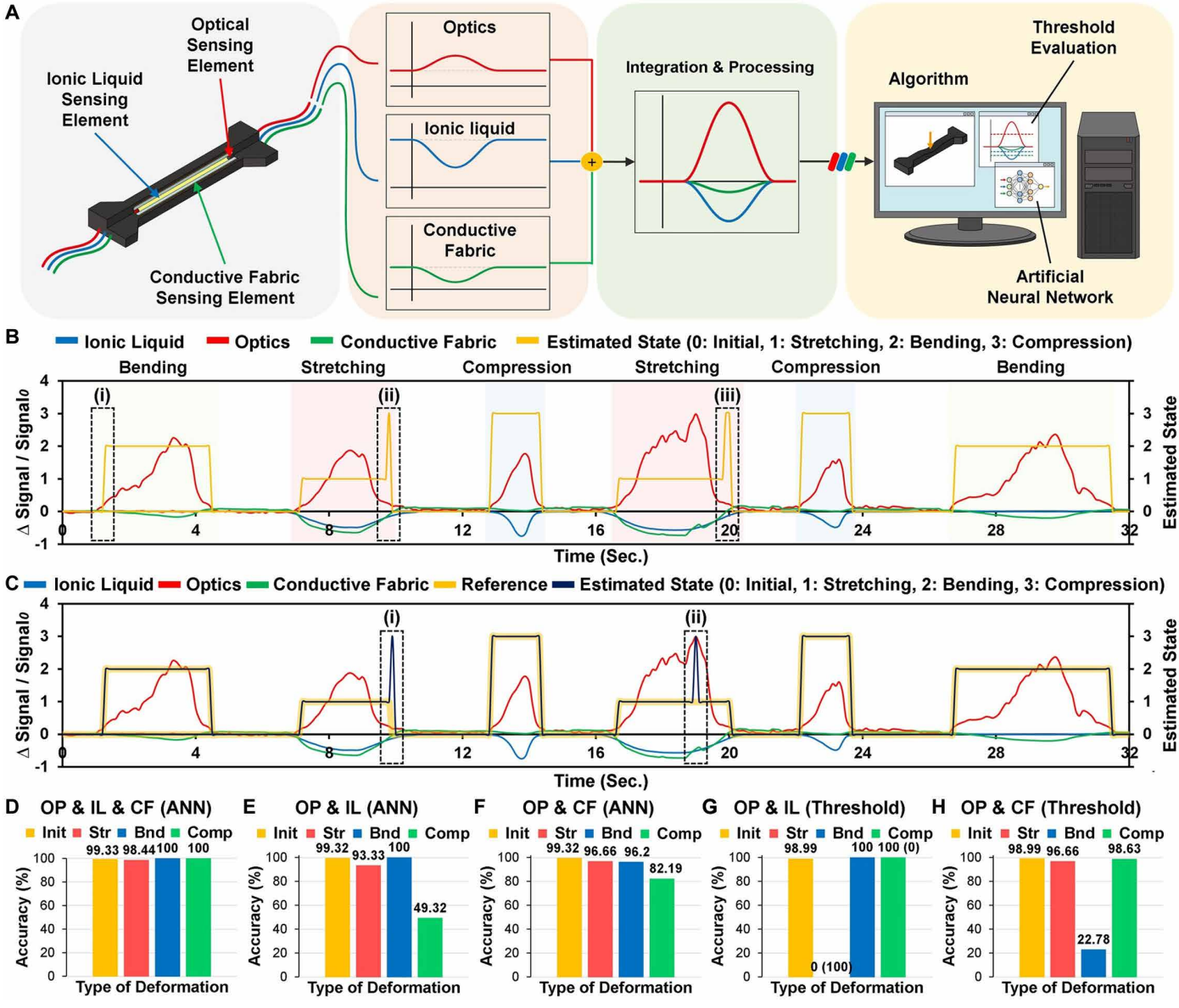

Fig. 4. Classification results of single-mode deformation sensing. (**A**) Overall process of deformation mode classification. (**B**) State estimation based on threshold evaluation. (i) to (iii) show errors at the boundaries of estimations. (**C**) State estimation using machine learning based on ANN. (i) and (ii) show errors at the boundary and in the middle of estimations, respectively. (**D** to **H**) Accuracy comparisons of state estimations for different combinations of multimode deformations using machine learning or threshold evaluation. Init, no deformation; Str, stretching; Bnd, bending; Comp, compression.

started responding to bending because the signal level is still lower than the threshold value (Fig. 4B, i). In addition, Fig. 4B (ii to iii) shows incorrect state estimation at the ends of the stretching events, because the signal from the conductive fabric reached the threshold value ahead of those from the optical and the RTIL sensing as the strain decreased. We noticed that the performance of a state estimation could be different depending on the sensitivity of each sensing element and the level of the threshold from the result.

Figure 4C is the result of using machine learning, showing a higher performance in estimating the input states (see movie S4). The difference from the threshold evaluation is that there was an estimation error at a boundary (Fig. 4C, i) and also in the middle of a state (Fig. 4C, ii) due to the sudden decrease in the signal from the conductive fabric. However, the ANN with all three sensing outputs estimated the input states with high accuracy in general, as shown in Fig. 4D.

We also tested the two algorithms only with two output signals to check the feasibility of fault tolerance. With the optical and the RTIL sensing signals only, the ANN showed high accuracies over 93% for estimating stretching and bending but a low accuracy for compression below 50% (Fig. 4E). The estimation accuracy for compression increased over 82% when the RTIL signal was replaced with the conductive fabric signal in the network (Fig. 4F). However, the threshold algorithm was not able to detect one of the three deformation states in either case. Stretching was not detected at all with optical and RTIL sensing only (Fig. 4G). The accuracy for estimating bending was only slightly over 22% when the optical and the conductive

fabric signals were used (Fig. 4H). We did not test the case when the optical signal was missing, because the optical sensing is responsive to and shows the highest sensitivity for all three deformation modes.

Multimode deformation

Because the output patterns for all three deformation modes are independent of each other, as shown in Figs. 1F and 2, we can decouple the combined deformation modes. However, the fact that not all the sensor signals are linear complicates the problem of decoupling and does not provide a simple solution by matrix calculation. Therefore, we decided to use a machine learning technique for the classification of multimode deformations. Figure 5A shows the estimated results for eight different deformation states (initial state: no deformation, three single-mode deformations, and four multimode deformations). In all cases, state estimations were highly accurate and reliable. The estimation accuracies were always over 95% (Fig. 5B). Movie S5 demonstrates the capability of detecting multimode deformations in real-time using the ANN-based machine learning algorithm. An additional test was conducted to check whether the sequence of deformations can affect the classification performance in multifunctional sensing. The result showed that classification accuracies were high and reliable regardless of the sequence of deformations if all deformation sequences were trained (see note S3 and fig. S12).

Applications for human-robot interface

To demonstrate the potential of the proposed sensor as a method for human-robot interfaces, we constructed two types of robotic systems integrated with sensor prototypes, as shown in fig. S13. The first system shows wearable devices (see fig. S14 and movie S6) for remotely controlling robots. The other is a soft robot that can detect deformation caused by its own actuation and external stimuli. Only one sensor is enough to control the system or detect deformation, because a single sensor had the capability to detect or represent multiple degrees of freedom (DoFs).

Wearable controller for robots

A pair of wearable sensing devices was prepared by attaching a sensor to the top side of a fabric wrist brace for each device (see fig. S15A) for detecting flexion (stretching) and yaw rotation (bending) of two wrists. Threshold evaluation was used to classify deformation modes. Flexion is detected by simultaneous stretching and bending of the sensor, whereas yaw rotation is detected by pure bending. When added by a compression mode in each device, 10 combination input modes in total are possible. We used 8 of the possible 10 modes (see fig. S15D) for remotely controlling a commercial robot arm with a gripper (RM-X52-TNM, ROBOTIS; see fig. S15B) for a task of picking up and moving an object to a target location (movie S7). In this system, yaw rotations of the left and the right wrists make the robot move to the left (Fig. 6, i) and to the right (Fig. 6, iii), respectively, and flexion of each wrist moves the robot either forward or backward. The compression on the sensor was used for moving the robot up and down (Fig. 6, ii and v, and gripping and releasing the object were conducted by flexing (Fig. 6, iv) and extending (Fig. 6, vi) both wrists at the same time, respectively. We used the same wearable controller to remotely control a small uncrewed aerial vehicle (sUAV) (CoDrone II Pro, Robolink) (see figs. S15, C and D, and S16 and movie S8). The task of taking off, moving in different directions, and landing of the sUAV was successfully carried out, as demonstrated in fig. S16 (i, ii to vii, and viii), respectively.

In addition, we implemented another wearable controller capable of measuring elbow angles to remotely control a robotic arm (UR5e, Universal Robots) that followed one-DoF elbow motions based on the calibrated optical signal, as shown in Fig. 7 (i) (see fig. S15, E to G). The sensor was able to estimate the wearer's elbow angle, and the robotic arm successfully tracked the wearer's motions. Furthermore, when an external contact was applied to the sensor, the system was able to effectively reject it. Thus, the motion of the robotic arm was not disturbed by the unwanted input signal, based on the deformation modes identified by the ANN-based machine learning algorithm, as shown in Fig. 7 (iii). This result confirms that the multifunctional sensing capability of the proposed sensor can be used to prevent the robot from malfunctioning by accidental unwanted inputs (see movie S9).

Interactive soft robotic manipulator

We implemented our sensor to a custom-built multi-DoF soft robotic wrist composed of four pneumatic origami muscle actuators (POMAs) (*85*), as shown in Fig. 8A. The robotic wrist was able to bend in different directions by pressurizing one or two POMAs and also extend its length when all four actuators are pressurized simultaneously. In this system, we placed our sensor in the middle of the four actuators, aligning it to the neutral axis so that the sensor can detect both bending and extension of the manipulator with different pressure inputs using threshold evaluation. In addition, the sensor

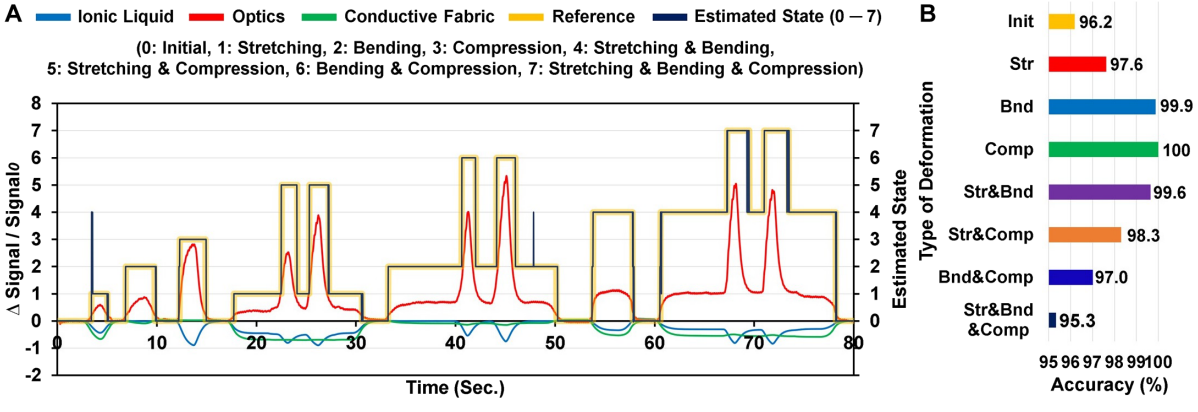

Fig. 5. Results of multifunctional sensing. (**A**) Estimation result using machine learning for eight different combinations of multimode deformations. (**B**) Estimation accuracies of all eight deformation modes.

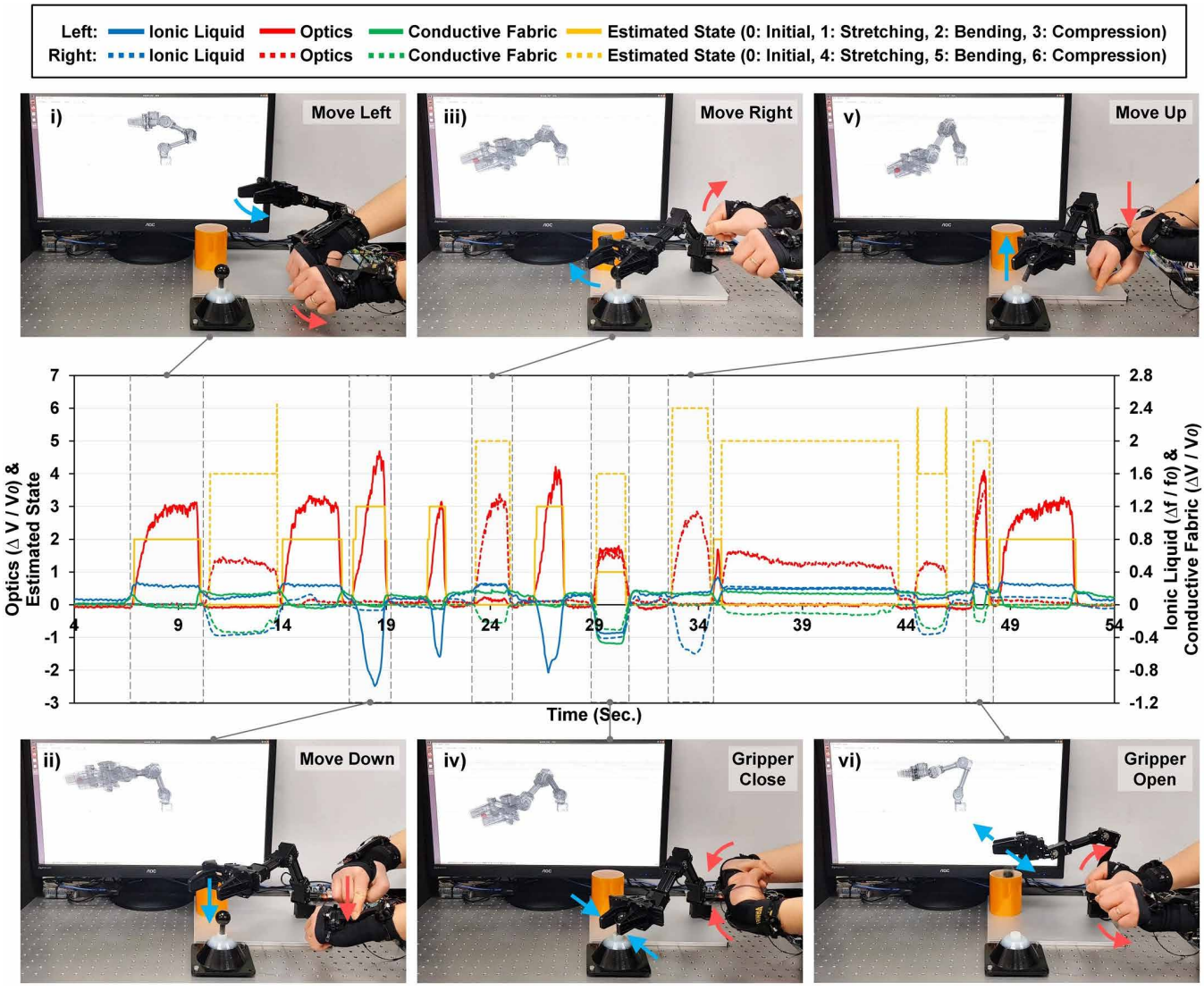

Fig. 6. Remote control of a robot arm with a gripper for different manipulation tasks and the corresponding sensor data. Two wearable devices were used to provide six different input modes necessary to move the robot and to pick up and release the object: (i) move left, (ii) move down, (iii) move right, (iv) gripper close, (v) move up, and (vi) gripper open.

was able to detect external forces applied to the robot because the soft structure can transmit the force to the sensor located inside. The results of sensing tests are shown in Fig. 8 (B to D) (see movie S10).

DISCUSSION

The main contribution of this work is the design and fabrication of a multifunctional soft sensor and its potential applications in the area of human-robot interaction and interfaces. Furthermore, we feel that the method of packaging heterogeneous sensing mechanisms in a single sensor structure is different compared with prior designs. Although there have been soft sensors proposed by different groups for multimodal sensing, the main idea of their mechanisms is to integrate multiple identical sensing elements with different configurations into one sensor, resulting in complexity in design and in fabrication (*11*, *70*). However, in our design, three heterogeneous sensing mechanisms were packaged in a single sensor. The heterogeneity enabled the three mechanisms to physically share a single structure for sensing, allowing for simplicity in design and fabrication and providing the compact form factor. This advantage becomes clearer when the proposed mechanism is compared with other methods of fabricating multimodal sensors in previous research (*11*, *69*, *70*). The proposed sensor has a substantially higher number of modalities with a similar or a smaller number of fabrication steps as summarized in table S2. The table S2 also shows that other methods require special care and equipment.

Despite the advantages of the proposed design, there is still room for further improvement. First, the current manufacturing process involves manual steps for placing electronic components and injecting the liquid conductor, which sometimes cause variations in the performance and the quality of the prototype, and requires a thorough calibration process for each sensor, which is time consuming. An automated manufacturing process, such as direct patterning of liquid conductors (*12*, *68*, *86*) or embedded 3D printing (*18*, *87*, *88*), will be highly useful to increase the uniformity of the product in this case. Furthermore, a transfer learning technique

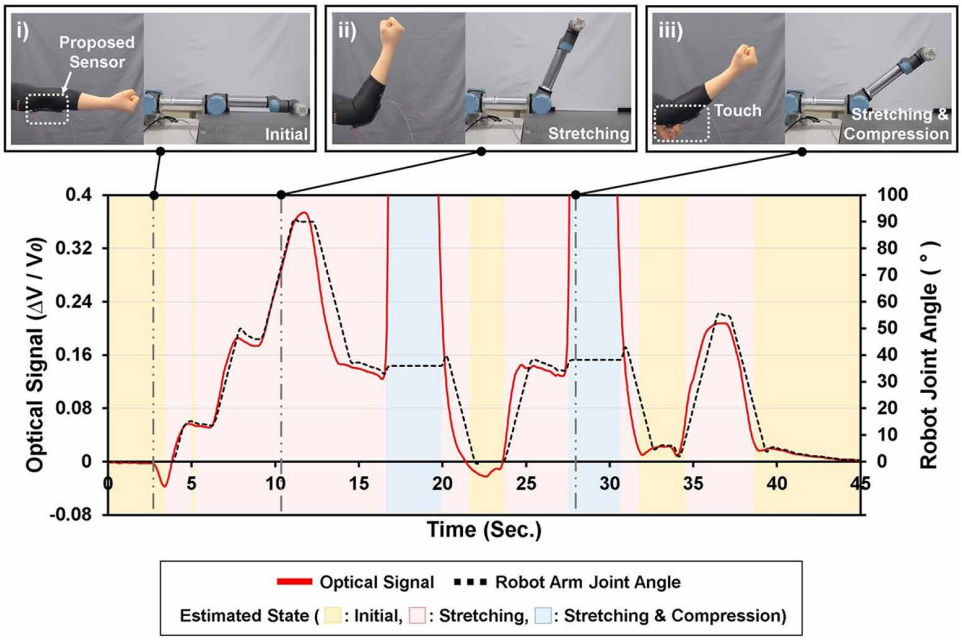

Fig. 7. Remote control of a commercial robotic arm using elbow joint motions calibrated by the optical signal. (i) Proposed soft sensor worn on the elbow in the initial state. (ii) Robotic arm after the flexion motion of the elbow. (iii) Robotic arm does not change its position although the sensor was compressed.

(*89*) can be used for calibrating multiple sensors with variations more efficiently, which will save a considerable amount of time and resources when compared with traditional calibration methods.

Optimization of design parameters is another area to focus on in the next stage. During testing, we found that parameters, such as the diameter of the waveguide, the thickness of the optical cladding, and the distance between the LED and the photodiode, have substantial influences on the performance of each sensing element. In this case, optimal parameter values can be found using methods of morphology optimization (*90*) and model-based computation (*91*), previously demonstrated for designing soft robotic grippers and proprioceptive soft robots, respectively.

We would also like to extend the capability of multifunctional sensing. Although the proposed sensor can detect eight different deformation modes composed of three individual modes (stretching, bending, and compression), the detection of additional input modes will always be useful if it does not complicate the design too much in the aspect of human-robot/machine interactions. One deformation mode that we are immediately interested to add is twisting, because torque is one of the most common forms of physical stimuli that humans can apply to devices. The conductive fabric layer located on the outside surface will be mostly affected by twisting caused by a pure torque. However, there will not be substantial changes in both optical and ionic liquid sensing. If we use the anisotropic property of the weaving pattern of the fabric, it will be even possible to detect the direction of the torque, as discussed in multidimensional strain sensors (*92*, *93*).

Another area of future work is to address the influence of the deformation locations, shown in fig. S7. Although it was confirmed that it was still possible to classify the deformation modes despite the fact that the location of deformation was changed, the estimated magnitude might not be the same. Possible solutions include embedding the sensor in the body of a soft robot and exposing only a specific area of the sensor to contacts or encapsulating the optical components with a rigid material. In this way, consistency in deformation can be structurally guaranteed.

Therefore, our future work includes the development of an automated fabrication process to minimize the manufacturing tolerances, the optimization of the design parameters for each sensing mechanism for maximizing the performance of the sensor, the extension of the sensing modalities with additional modes such as twisting, and addressing the influence of the deformation locations to improve consistency in deformation.

MATERIALS AND METHODS

Fabrication of sensing structure

The proposed sensor can be easily fabricated by a simple molding and casting process by virtue of its structural simplicity. The body of the waveguide was fabricated by casting liquid silicone elastomer (SORTA-Clear 12, Smooth-On) in a 3D printed (Objet30 Prime, Stratasys) mold. An aluminum shaft was placed at the center of the mold as an inner mold to form a hollow channel before pouring the elastomer (fig. S17A). Once the body cured, an LED (3R4UC8-02, HSUKWANG) and a photodiode (ST-3811, AUK) were inserted and glued at the ends of the channel, closing the open ends (fig. S17B). The hollow channel was then filled with RTIL (1-ethyl-3-methylimidazolium ethyl sulfate, Alfa Aesar) using syringes, and signal wires were connected (fig. S17, C and D). The next step is the lamination of a conductive fabric layer (Medtex P130, V Technical Textile Inc.) outside the elastomer body (fig. S17E). Last, holders at both ends for testing and the cover layer of the sensor were formed with different elastomers (SORTA-Clear 40 and Ecoflex 00-30, respectively, Smooth-On) (fig. S17, F and G). Both materials are nontransparent. A final prototype of the proposed multifunctional soft sensor is shown in fig. S17H.

Simulation environment

We ran an FEA simulation on mechanical, electrical, and optical responses of the proposed sensor corresponding to each physical deformation (stretching, bending, and compression) using a commercial FEA software package (COMSOL Multiphysics).

To apply stretching deformation to the waveguide structure, shared by the ionic liquid channel, one end of the structure was fixed, and the other end was pulled along the length of the sensor until the strain reached 50% of the initial length (66 mm). For bending, moments were applied to both ends until the curvature of the sensor reached 0.05 mm^{-1}. For compression, the bottom surface was fixed, and a local contact pressure up to 110 kPa was applied to the top surface of the structure. In the case of the conductive fabric layer, the same stretching, bending, and compression deformations

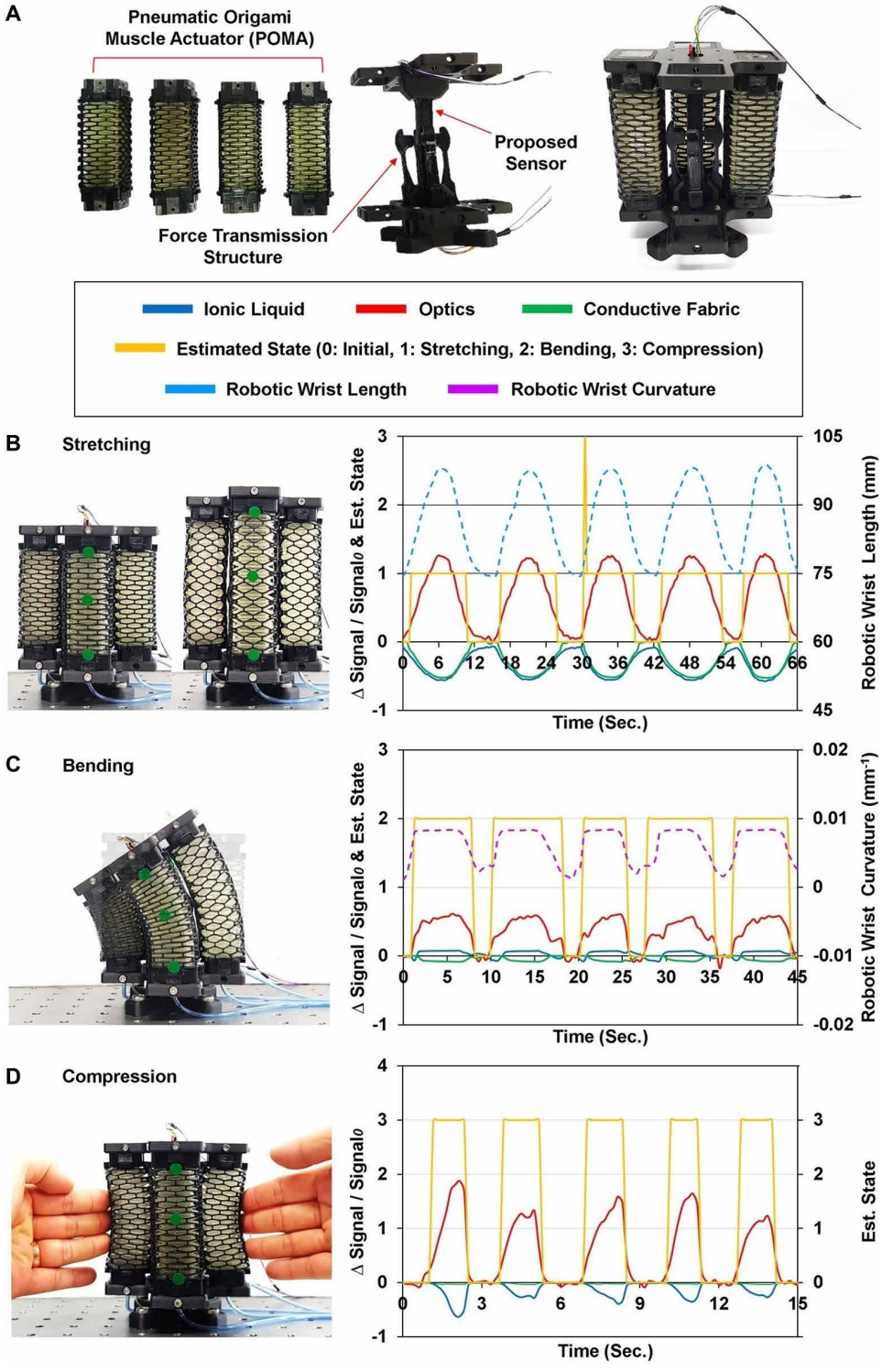

Fig. 8. Multi-DoF soft interactive robot. (**A**) Design of the robot composed of four pneumatic actuators and a single soft sensor. (**B** to **D**) Different deformation modes by self-actuation as well as human inputs and corresponding sensor data.

Readout circuit

A custom-designed sensor readout circuit was prepared for the experiments (see fig. S18 and note S5). The electrical system can be broken into three parts: a waveform generator, three sensing elements, and a data acquisition unit. The AC waveform generator was necessary for measuring the signal from the ionic liquid channel. If a DC is applied to the channel, electrolytic polarization occurs at the metallic electrodes, because the conductivity of the liquid channel is formed by the movements of ions in the solution. This will result in the loss of conductivity as the ions in the liquid are electrolyzed. An AC input signal was, therefore, applied instead to prevent electrolysis.

Test setups for characterization

Single-mode deformation

An automated sensor testbed was built using a motorized three-axis (*x*-*y*-*z*) stage for characterizing single-mode deformation (fig. S3). The testbed had three testing modules for stretching, bending, and compression tests, individually, which facilitated collecting data from the sensors with controlled speeds and setting the number of test cycles. To minimize the error caused by slip during testing, the holders at the ends of the sensor were firmly clamped at the jigs. The stage moved at 2 mm/s for all tests, and the sensor data were collected for 10 cycles in each test. Repeatability and durability were also evaluated by loading-unloading testing with 200 cycles for each sensing element.

Multimode deformation

For the characterization of multimode deformation sensing, another automated testbed was prepared and installed in the same motorized stage with additional test modules (fig. S19). The deformation of combined stretching and compression was created by applying a local contact pressure up to 573 kPa to the sensor that was already stretched by 50% (fig. S19A). Deformation of the combined stretching and bending mode applied by the setup (fig. S19B) generated strain and curvature up to 23% and 0.020 mm^{-1}, respectively. For this combined bending and compression testing, the sensor was compressed up to 238 kPa after it was purely bent with a curvature of 0.025 mm^{-1} without stretching (fig. S19C). Last, the deformation with all three modes combined was created by locally

were applied to a simplified 3D model of the fabric with the same conditions for the optical and ionic liquid responses (see note S4 for more details on the simulation methods).

compressing (up to 238 kPa) the prestretched and prebent (23% and 0.020 mm^{-1}, respectively) sensor (fig. S19D).

Classification algorithms

Single-mode deformation

It is possible to distinguish the types of input deformations to the sensor based on different output signal patterns. Three different deformation modes were estimated (0, initial; 1, stretching; 2, bending; and 3, compression) using a simple algorithm based on threshold evaluation (see fig. S10 and note S6).

A machine learning algorithm based on an ANN (see fig. S11 and note S7) was also implemented to estimate the types of input deformations. The training data were collected by stretching, compressing, and bending the sensor in random ranges of strain, pressure, and curvature, respectively, for 50 cycles. Additional trials were then performed to collect the test data. The reference of the deformation states for the training and the test datasets was determined with the state results estimated by the above threshold evaluation algorithm.

Multimode deformation

Although the threshold evaluation method was accurate enough to estimate the deformation states for single-mode deformation sensing, it was not able to effectively decouple combined deformation modes. Therefore, the ANN-based machine learning method was used. The architecture of the ANN model had one more hidden layer than that used for single-mode sensing, and the parameter values were reset (see note S8).

SUPPLEMENTARY MATERIALS

robotics.sciencemag.org/cgi/content/full/5/49/eabc6878/DC1
Note S1. State of the art of multimodal sensing structures.
Note S2. Influence of temperature on the ionic liquid signal.
Note S3. Influence of deformation sequence on the mode classification.
Note S4. Simulation setup.
Note S5. Readout circuit.
Note S6. Threshold evaluation for detecting single-mode deformation.
Note S7. ANN architecture for detecting single-mode deformations.
Note S8. ANN architecture for decoupling multimode deformations.
Fig. S1. Microscopic images showing the shape changes of weaving patterns of the conductive fabric depending on different deformation states.
Fig. S2. Simulation results of all three sensing mechanisms with different deformation inputs.
Fig. S3. Sensor characterization setup for single-mode deformation testing.
Fig. S4. Cyclic test results of loading and unloading loops for 200 cycles.
Fig. S5. Calibration result of optical sensing signals.
Fig. S6. Bending and compression tests on different deformation locations.
Fig. S7. Results of bending and compression tests on different deformation locations.
Fig. S8. Experimental setup for thermal characterization of the ionic liquid sensor.
Fig. S9. Temperature sensitivity of the ionic liquid sensor for 1500 s with different temperature conditions.
Fig. S10. Classification algorithm for estimating single-mode deformations based on threshold evaluation.
Fig. S11. Architecture of the ANN used for estimating single-mode deformation.
Fig. S12. Classification result of multimode deformation applied in different sequences.
Fig. S13. Application examples of human-robot interfaces.
Fig. S14. System configurations of the wearable sensing devices.
Fig. S15. Wearable controller application setup.
Fig. S16. Demonstration of remote control of the sUAV for different motion tasks and the corresponding sensor data.
Fig. S17. Fabrication process.
Fig. S18. Sensor signal readout circuit.
Fig. S19. Test setups for multimode deformation sensing.
Table S1. Characteristic of optical signals.
Table S2. Comparison between the fabrication process of the proposed sensor and existing multimodal sensors.
Table S3. Summary of the state of the art of multimodal sensing structures.
Movie S1. FEA simulation of three sensing mechanisms.
Movie S2. Characterization of single-mode deformation.
Movie S3. Characterization of multimode deformation.
Movie S4. Sensing of single-mode deformations.
Movie S5. Sensing of multimode deformations.
Movie S6. Wearable device for wrist and elbow motion sensing.
Movie S7. Remote manipulation of the robotic arm with a gripper.
Movie S8. Remote control of the uncrewed aerial vehicle.
Movie S9. Remote control of the commercial robotic arm and contact recognition.
Movie S10. Interactive multi-DoF soft robot.
Reference (*94*)

REFERENCES AND NOTES

1. N. W. Bartlett, M. T. Tolley, J. T. B. Overvelde, J. C. Weaver, B. Mosadegh, K. Bertoldi, G. M. Whitesides, R. J. Wood, A 3D-printed, functionally graded soft robot powered by combustion. *Science* **349**, 161–165 (2015).
2. N. S. Usevitch, Z. M. Hammond, M. Schwager, A. M. Okamura, E. W. Hawkes, S. Follmer, An untethered isoperimetric soft robot. *Sci. Robot.* **5**, eaaz0492 (2020).
3. E. W. Hawkes, L. H. Blumenschein, J. D. Greer, A. M. Okamura, A soft robot that navigates its environment through growth. *Sci. Robot.* **2**, eaan3028 (2017).
4. C. Christianson, N. N. Goldberg, D. D. Deheyn, S. Cai, M. T. Tolley, Translucent soft robots driven by frameless fluid electrode dielectric elastomer actuators. *Sci. Robot.* **3**, eaat1893 (2018).
5. M. T. Tolley, R. F. Shepherd, B. Mosadegh, K. C. Galloway, M. Wehner, M. Karpelson, R. J. Wood, G. M. Whitesides, A resilient, untethered soft robot. *Soft robot.* **1**, 213–223 (2014).
6. A. A. Stokes, R. F. Shepherd, S. A. Morin, F. Ilievski, G. M. Whitesides, A hybrid combining hard and soft robots. *Soft Robot.* **1**, 70–74 (2014).
7. Y.-L. Park, B. R. Chen, N. O. Pérez-Arancibia, D. Young, L. Stirling, R. J. Wood, E. C. Goldfield, R. Nagpal, Design and control of a bio-inspired soft wearable robotic device for ankle–foot rehabilitation. *Bioinspir. Biomim.* **9**, 016007 (2014).
8. T. Kim, S. J. Yoon, Y.-L. Park, Soft inflatable sensing modules for safe and interactive robots. *IEEE Robot. Autom. Lett.* **3**, 3216–3223 (2018).
9. M. Maselli, E. Mussi, F. Cecchi, M. Manti, P. Tropea, C. Laschi, A wearable sensing device for monitoring single planes neck movements: Assessment of its performance. *IEEE Sens. J.* **18**, 6327–6336 (2018).
10. Y. Ansari, M. Manti, E. Falotico, Y. Mollard, M. Cianchetti, C. Laschi, Towards the development of a soft manipulator as an assistive robot for personal care of elderly people. *Int. J. Adv. Robot. Syst.* **14**, 10.1177/1729881416687132, (2017).
11. Y.-L. Park, B. Chen, R. J. Wood, Design and fabrication of soft artificial skin using embedded microchannels and liquid conductors. *IEEE Sens. J.* **12**, 2711–2718 (2012).
12. G. Shin, B. Jeon, Y.-L. Park, Direct printing of sub-30 μm liquid metal patterns on three-dimensional surfaces for stretchable electronics. *J. Micromech. Microeng.* **30**, 034001 (2020).
13. S. Kim, J. Oh, D. Jeong, J. Bae, Direct wiring of eutectic gallium-indium to a metal electrode for soft sensor systems. *ACS Appl. Mater. Interfaces* **11**, 20557–20565 (2019).
14. J. Yin, V. J. Santos, J. D. Posner, Bioinspired flexible microfluidic shear force sensor skin. *Sens. Actuators, A Phys.* **264**, 289–297 (2017).
15. J. Yin, P. Aspinall, V. J. Santos, J. D. Posner, Measuring dynamic shear force and vibration with a bioinspired tactile sensor skin. *IEEE Sens. J.* **18**, 3544–3553 (2018).
16. T. Kim, Y.-L. Park, A soft 3-axis load cell using liquid-filled three-dimensional microchannels in a highly deformable elastomer. *IEEE Robot. Autom. Lett.* **3**, 881–887 (2018).
17. B. Li, Y. Gao, A. Fontecchio, Y. Visell, Soft capacitive tactile sensing arrays fabricated via direct filament casting. *Smart Mater. Struct.* **25**, 075009 (2016).
18. A. Frutiger, J. T. Muth, D. M. Vogt, Y. Mengüç, A. Campo, A. D. Valentine, C. J. Walsh, J. A. Lewis, Capacitive soft strain sensors via multicore–shell fiber printing. *Adv. Mater.* **27**, 2440–2446 (2015).
19. E. P. Yalcintas, K. B. Ozutemiz, T. Cetinkaya, L. Dalloro, C. Majidi, O. B. Ozdoganlar, Soft electronics manufacturing using microcontact printing. *Adv. Funct. Mater.* **29**, 1906551 (2019).
20. H. Shi, M. Al-Rubaiai, C. M. Holbrook, J. Miao, T. Pinto, C. Wang, X. Tan, Screen-printed soft capacitive sensors for spatial mapping of both positive and negative pressures. *Adv. Funct. Mater.* **29**, 1809116 (2019).
21. O. Atalay, A. Atalay, J. Gafford, C. Walsh, A highly sensitive capacitive-based soft pressure sensor based on a conductive fabric and a microporous dielectric layer. *Adv. Mater. Technol.* **3**, 1700237 (2018).
22. R. P. Rocha, P. A. Lopes, A. T. de Almeida, M. Tavakoli, C. Majidi, Fabrication and characterization of bending and pressure sensors for a soft prosthetic hand. *J. Micromech. Microeng.* **28**, 034001 (2018).

23. C. Larson, B. Peele, S. Li, S. Robinson, M. Totaro, L. Beccai, B. Mazzolai, R. Shepherd, Highly stretchable electroluminescent skin for optical signaling and tactile sensing. *Science* **351**, 1071–1074 (2016).
24. J. Guo, X. Liu, N. Jiang, A. K. Yetisen, H. Yuk, C. Yang, A. Khademhosseini, X. Zhao, S.-H. Yun, Highly stretchable, strain sensing hydrogel optical fibers. *Adv. Mater.* **28**, 10244–10249 (2016).
25. P. A. Xu, A. K. Mishra, H. Bai, C. A. Aubin, L. Zullo, R. F. Shepherd, Optical lace for synthetic afferent neural networks. *Sci. robot.* **4**, eaaw6304 (2019).
26. H. Zhao, K. O'Brien, S. Li, R. F. Shepherd, Optoelectronically innervated soft prosthetic hand via stretchable optical waveguides. *Sci. Robot.* **1**, eaai7529 (2016).
27. S. Yun, S. Park, B. Park, Y. Kim, S. K. Park, S. Nam, K.-U. Kyung, Polymer-waveguide-based flexible tactile sensor array for dynamic response. *Adv. Mater.* **26**, 4474–4480 (2014).
28. A. Samusjew, M. Kratzer, A. Moser, C. Teichert, K. K. Krawczyk, T. Griesser, Inkjet printing of soft, stretchable optical waveguides through the photopolymerization of high-profile linear patterns. *ACS Appl. Mater. Interfaces* **9**, 4941–4947 (2017).
29. L. Xu, N. Liu, J. Ge, X. Wang, M. P. Fok, Stretchable fiber-Bragg-grating-based sensor. *Opt. Lett.* **43**, 2503–2506 (2018).
30. A. Leal-Junior, V. Campos, A. Frizera, C. Marques, Low-cost and high-resolution pressure sensors using highly stretchable polymer optical fibers. *Mater. Lett.* **271**, 127810 (2020).
31. M. Yang, Q. Liu, H. S. Naqawe, M. P. Fok, Movement detection in soft robotic gripper using sinusoidally embedded fiber optic sensor. *Sensors* **20**, 1312 (2020).
32. W. Zhuang, G. Sun, H. Li, X. Lou, M. Dong, L. Zhu, FBG based shape sensing of a silicone octopus tentacle model for soft robotics. *Optik* **165**, 7–15 (2018).
33. J.-Y. Sun, C. Keplinger, G. M. Whitesides, Z. Suo, Ionic skin. *Adv. Mater.* **26**, 7608–7614 (2014).
34. J.-B. Chossat, H.-S. Shin, Y.-L. Park, V. Duchaine, Soft tactile skin using an embedded ionic liquid and tomographic imaging. *J. Mech. Robot.* **7**, 021008 (2015).
35. S. Russo, T. Ranzani, H. Liu, S. Nefti-Meziani, K. Althoefer, A. Menciassi, Soft and stretchable sensor using biocompatible electrodes and liquid for medical applications. *Soft Robot.* **2**, 146–154 (2015).
36. L. M. Zhang, Y. He, S. Cheng, H. Sheng, K. Dai, W. J. Zheng, M. X. Wang, Z. S. Chen, Y. M. Chen, Z. Suo, Self-healing, adhesive, and highly stretchable ionogel as a strain sensor for extremely large deformation. *Small* **15**, 1804651 (2019).
37. D. Y. Choi, M. H. Kim, Y. S. Oh, S.-H. Jung, J. H. Jung, H. J. Sung, H. W. Lee, H. M. Lee, Highly stretchable, hysteresis-free ionic liquid-based strain sensor for precise human motion monitoring. *ACS Appl. Mater. Interfaces* **9**, 1770–1780 (2017).
38. S. Chen, H. Liu, S. Liu, P. Wang, S. Zeng, L. Sun, L. Liu, Transparent and waterproof ionic liquid-based fibers for highly durable multifunctional sensors and strain-insensitive stretchable conductors. *ACS Appl. Mater. Interfaces* **10**, 4305–4314 (2018).
39. Z. Wang, Y. Si, C. Zhao, D. Yu, W. Wang, G. Sun, Flexible and washable poly (ionic liquid) nanofibrous membrane with moisture proof pressure sensing for real-life wearable electronics. *ACS Appl. Mater. Interfaces* **11**, 27200–27209 (2019).
40. R. C. Chiechi, E. A. Weiss, M. D. Dickey, G. M. Whitesides, Eutectic gallium–indium (EGaIn): A moldable liquid metal for electrical characterization of self-assembled monolayers. *Angew. Chem. Int. Ed.* **47**, 142–144 (2007).
41. M. D. Dickey, R. C. Chiechi, R. J. Larsen, E. A. Weiss, D. A. Weitz, G. M. Whitesides, Eutectic gallium-indium (EGaIn): A liquid metal alloy for the formation of stable structures in microchannels at room temperature. *Adv. Funct. Mater.* **18**, 1097–1104 (2008).
42. K. B. Ozutemiz, J. Wissman, O. B. Ozdoganlar, C. Majidi, EGaIn–metal interfacing for liquid metal circuitry and microelectronics integration. *Adv. Mater. Interfaces* **5**, 1701596 (2018).
43. A. Tabatabai, A. Fassler, C. Usiak, C. Majidi, Liquid-phase gallium–indium alloy electronics with microcontact printing. *Langmuir* **29**, 6194–6200 (2013).
44. Y. Lu, Q. Hu, Y. Lin, D. B. Pacardo, C. Wang, W. Sun, F. S. Ligler, M. D. Dickey, Z. Gu, Transformable liquid-metal nanomedicine. *Nat. Commun.* **6**, 10066 (2015).
45. E. Roh, B.-U. Hwang, D. Kim, B.-Y. Kim, N.-E. Lee, Stretchable, transparent, ultrasensitive, and patchable strain sensor for human-machine interfaces comprising a nanohybrid of carbon nanotubes and conductive elastomers. *ACS Nano* **9**, 6252–6261 (2015).
46. S. Lee, A. Reuveny, J. Reeder, S. Lee, H. Jin, Q. Liu, T. Yokota, T. Sekitani, T. Isoyama, Y. Abe, Z. Suo, T. Someya, A transparent bending-insensitive pressure sensor. *Nat. Nanotechnol.* **11**, 472–478 (2016).
47. K. A. Dubey, R. K. Mondal, J. Kumar, J. S. Melo, Y. K. Bhardwaj, Enhanced electromechanics of morphology-immobilized co-continuous polymer blend/carbon nanotube high-range piezoresistive sensor. *Chem. Eng. J.* **389**, 124112 (2020).
48. S.-H. Min, G.-Y. Lee, S.-H. Ahn, Direct printing of highly sensitive, stretchable, and durable strain sensor based on silver nanoparticles/multi-walled carbon nanotubes composites. *Compos. Part B Eng.* **161**, 395–401 (2019).
49. S. Yu, X. Wang, H. Xiang, L. Zhu, M. Tebyetekerwa, M. Zhu, Superior piezoresistive strain sensing behaviors of carbon nanotubes in one-dimensional polymer fiber structure. *Carbon* **140**, 1–9 (2018).
50. S. Gong, W. Schwalb, Y. Wang, Y. Chen, Y. Tang, J. Si, B. Shirinzadeh, W. Cheng, A wearable and highly sensitive pressure sensor with ultrathin gold nanowires. *Nat. Commun.* **5**, 3132 (2014).
51. S. Lee, S. Shin, S. Lee, J. Seo, J. Lee, S. Son, H. J. Cho, H. Algadi, S. Al-Sayari, D. E. Kim, T. Lee, Ag nanowire reinforced highly stretchable conductive fibers for wearable electronics. *Adv. Funct. Mater.* **25**, 3114–3121 (2015).
52. S. Yao, Y. Zhu, Wearable multifunctional sensors using printed stretchable conductors made of silver nanowires. *Nanoscale* **6**, 2345–2352 (2014).
53. H. S. Jo, S. An, C.-W. Park, D.-Y. Woo, A. L. Yarin, S. S. Yoon, Wearable, stretchable, transparent all-in-one soft sensor formed from supersonically sprayed silver nanowires. *ACS Appl. Mater. Interfaces* **11**, 40232–40242 (2019).
54. H. Lee, S. Hong, J. Lee, Y. D. Suh, J. Kwon, H. Moon, H. Kim, J. Yeo, S. H. Ko, Highly stretchable and transparent supercapacitor by Ag–Au core–shell nanowire network with high electrochemical stability. *Appl. Mater. Interfaces.* **8**, 15449–15458 (2016).
55. Y. Ling, S. Gong, Q. Zhai, Y. Wang, Y. Zhao, M. Yang, W. Cheng, Embedding pinhole vertical gold nanowire electronic skins for braille recognition. *Small* **15**, 1804853 (2019).
56. A. Atalay, V. Sanchez, O. Atalay, D. M. Vogt, F. Haufe, R. J. Wood, C. J. Walsh, Batch fabrication of customizable silicone textile composite capacitive strain sensors for human motion tracking. *Adv. Mater. Technol.* **2**, 1700136 (2017).
57. A. Nag, R. B. V. B. Simorangkir, E. Valentin, T. Björninen, L. Ukkonen, R. M. Hashmi, S. C. Mukhopadhyay, A transparent strain sensor based on PDMS-embedded conductive fabric for wearable sensing applications. *IEEE Access.* **6**, 71020–71027 (2018).
58. T. Matsuno, Z. Wang, K. Althoefer, S. Hirai, Adaptive update of reference capacitances in conductive fabric based robotic skin. *IEEE Robot. Autom. Lett.* **4**, 2212–2219 (2019).
59. I. Baldoli, M. Maselli, F. Cecchi, C. Laschi, Development and characterization of a multilayer matrix textile sensor for interface pressure measurements. *Smart Mater. Struct.* **26**, 104011 (2017).
60. Y.-L. Park, C. Majidi, R. Kramer, P. Bérard, R. J. Wood, Hyperplastic pressure sensing with a liquid-embedded elastomer. *J. Micromech. Microeng.* **20**, 125029 (2010).
61. J.-B. Chossat, Y.-L. Park, R. J. Wood, V. Duchaine, A soft strain sensor based on ionic and metal liquids. *IEEE Sens. J.* **13**, 3405–3414 (2013).
62. S. G. Yoon, B. J. Park, S. T. Chang, Highly sensitive microfluidic strain sensors with low hysteresis using a binary mixture of ionic liquid and ethylene glycol. *Sens. Actuators, A Phys.* **254**, 1–8 (2017).
63. Y. Mengüç, Y.-L. Park, H. Pei, D. Vogt, P. M. Aubin, E. Winchell, L. Fluke, L. Stirling, R. J. Wood, C. J. Walsh, Wearable soft sensing suit for human gait measurement. *Int. J. Robot. Res.* **33**, 1748–1764 (2014).
64. J. Jung, M. Park, D. Kim, Y.-L. Park, Optically sensorized elastomer air chamber for proprioceptive sensing of soft pneumatic actuator. *IEEE Robot. Autom. Lett.* **5**, 2333–2340 (2020).
65. C. To, T. Hellebrekers, J. Jung, S. J. Yoon, Y.-L. Park, A soft optical waveguide coupled with fiber optics for dynamic pressure and strain sensing. *IEEE Robot. Autom. Lett.* **3**, 3821–3827 (2018).
66. C. Lucarotti, M. Totaro, A. Sadeghi, B. Mazzolai, L. Beccai, Revealing bending and force in a soft body through a plant root inspired approach. *Sci. Rep.* **5**, 8788 (2015).
67. H. Wang, M. Totaro, L. Beccai, Toward perceptive soft robots: Progress and challenges. *Adv. Sci.* **5**, 1800541 (2018).
68. R. L. Truby, M. Wehner, A. K. Grosskopf, D. M. Vogt, S. G. M. Uzel, R. J. Wood, J. A. Lewis, Soft somatosensitive actuators via embedded 3D printing. *Adv. Materials* **30**, 1706383 (2018).
69. E. L. White, J. C. Case, R. K. Kramer, Multi-mode strain and curvature sensors for soft robotic applications. *Sens. Actuators A Phys.* **253**, 188–197 (2017).
70. S. Din, W. Xu, L. K. Cheng, S. Dirven, A stretchable multimodal sensor for soft robotic applications. *IEEE Sens. J.* **17**, 5678–5686 (2017).
71. T. G. Thuruthel, B. Shih, C. Laschi, M. T. Tolley, Soft robot perception using embedded soft sensors and recurrent neural networks. *Sci. Robot.* **4**, eaav1488 (2019).
72. M. Totaro, A. Mondini, A. Bellacicca, P. Milani, L. Beccai, Integrated simultaneous detection of tactile and bending cues for soft robotics. *Soft Robot.* **4**, 400–410 (2017).
73. Y. Yang, Y. Chen, Innovative design of embedded pressure and position sensors for soft actuators. *IEEE Robot. Autom. Lett.* **3**, 656–663 (2018).
74. J. S. Weszka, A. Rosenfeld, Threshold evaluation techniques. *IEEE Trans. Syst. Man. Cybern.* **8**, 622–629 (1978).
75. A. K. Bourke, J. V. O'Brien, G. M. Lyons, Evaluation of a threshold-based tri-axial accelerometer fall detection algorithm. *Gait Posture* **26**, 194–199 (2007).
76. D. H. Nguyen, B. Widrow, Neural networks for self-learning control systems. *IEEE Contr. Syst. Mag.* **10**, 18–23 (1990).
77. D. E. Rumelhart, B. Widrow, M. A. Lehr, The basic ideas in neural networks. *Commun. ACM.* **37**, 87–93 (1994).
78. S. Han, T. Kim, D. Kim, Y.-L. Park, S. Jo, Use of deep learning for characterization of microfuidic soft sensors. *IEEE Robot. Autom. Lett.* **3**, 873–880 (2018).
79. H.-S. Shin, J. Ryu, C. Majidi, Y.-L. Park, Enhanced performance of microfluidic soft pressure sensors with embedded solid microspheres. *J. Micromech. Microeng.* **26**, 025011 (2016).

80. Y.-L. Park, D. Tepayotl-Ramirez, R. J. Wood, C. Majidi, Influence of cross-sectional geometry on the sensitivity of liquid-phase electronic pressure sensors. *Appl. Phys. Lett.* **101**, 191904 (2012).
81. H. O. Spivey, T. Shedlovsky, Studies of electrolytic conductance in alcohol-water mixtures. I. Hydrochloric acid, sodium chloride, and sodium acetate at 0, 25, and 35. degree. in ethanol-water mixtures. *J. Phys. Chem.* **71**, 2165–2171 (1967).
82. J. J. Barron, C. Ashton, The effect of temperature on conductivity measurement. *TSP* **7**, 1–5 (2005).
83. X. Yang, Y. Wang, X. Qing, A flexible capacitive pressure sensor based on ionic liquid. *Sensors* **18**, 2395 (2018).
84. C.-Y. Wu, W.-H. Liao, Y.-C. Tung, Integrated ionic liquid-based electrofluidic circuits for pressure sensing within polydimethylsiloxane microfluidic systems. *Lab Chip* **11**, 1740–1746 (2011).
85. T. Hong, Y.-L. Park, Design of pneumatic origami muscle actuators (POMAs) for a soft robotic hand orthosis for grasping assistance, in *Proceedings of the IEEE International Conference on Soft Robotics (RoboSoft 2020)*, New Haven, USA, 2020 (IEEE, 2020).
86. W. Boley, E. L. White, G. T.-C. Chiu, R. K. Kramer, Direct writing of gallium-indium alloy for stretchable electronics. *Adv. Funct. Mater.* **24**, 3501–3507 (2014).
87. M. Wehner, R. L. Truby, D. J. Fitzgerald, B. Mosadegh, G. M. Whitesides, J. A. Lewis, R. J. Wood, An integrated design and fabrication strategy for entirely soft, autonomous robots. *Nature* **536**, 451–455 (2016).
88. J. T. Muth, D. M. Vogt, R. L. Truby, Y. Mengüç, D. B. Kolesky, R. J. Wood, J. A. Lewis, Embedded 3D printing of strain sensors within highly stretchable elastomers. *Adv. Mater.* **26**, 6307–6312 (2014).
89. D. Kim, J. Kwon, B. Jeon, Y.-L. Park, Adaptive calibration of soft sensors using optimal transportation transfer learning for mass production and long-term usage. *Adv. Intell. Syst.* **2**, 1900178 (2020).
90. H. Zhang, A. S. Kumar, J. Y. H. Fuh, M. Y. Wang, Design and development of a topology-optimized three-dimensional printed soft gripper. *Soft Robot.* **5**, 650–661 (2018).
91. J. Tapia, E. Knoop, M. Mutný, M. A. Otaduy, M. Bächer, MakeSense: Automated sensor design for proprioceptive soft robots. *Soft Robot.* **7**, 332–345 (2019).
92. K. K. Kim, S. Hong, H. M. Cho, J. Lee, Y. D. Suh, J. Ham, S. H. Ko, Highly sensitive and stretchable multidimensional strain sensor with prestrained anisotropic metal nanowire percolation networks. *Nano Lett.* **15**, 5240–5247 (2015).
93. H. Nakamoto, H. Ootaka, M. Tada, I. Hirata, F. Kobayashi, F. Kojima, Stretchable strain sensor with anisotropy and application for joint angle measurement. *IEEE Sens. J.* **16**, 3572–3579 (2016).
94. M. Kahnert, Modelling the optical and radiative properties of freshly emitted light absorbing carbon within an atmospheric chemical transport model. *Atmos. Chem. Phys.* **10**, 1403–1416 (2010).

Funding: This work was supported by the National Research Foundation (NRF) grants (NRF-2016R1A5A1938472 and NRF-2019-Global Ph.D. Fellowship Program) funded by the Korean government (MSIT). **Author contributions:** Taekyoung Kim proposed the design and the mechanism, fabricated the prototypes, and prepared the experimental setups. Taekyoung Kim also conducted data collection and analysis for all the experiments, implemented the machine learning algorithm, and demonstrated the performance of sensing and deformation classification. Last, Taekyoung Kim designed the experiments of the wearable sensing devices and the multi-DoF soft robot, fabricated the wearable devices, designed the multi-DoF soft robot, and wrote the manuscript. S.L. analyzed and processed the sensor data, implemented the threshold evaluation algorithm, and prepared the experimental setup for robotic arm manipulation and sUAV control applications. S.L. also implemented a 3D sensor model using MATLAB and an online learning platform using the trained ANN model. T.H. designed, fabricated the prototype of the multi-DoF soft robot, and prepared the experimental setup. G.S. conducted the FEA simulation and wrote the related section. Taehwan Kim assisted in preparing the experimental setups for the applications, the Supplementary Materials, and the graphical presentation of figures. Y.-L.P. directed the overall research and organized and wrote the manuscript. All authors responded to revisions in the review process. **Competing interests:** Taekyoung Kim, S.L., and Y.-L.P. are included in a Korea patent application (KR 10-2020-0144246) that covers the design and multifunctionality of the proposed heterogeneous sensor, which has been submitted by the SNU R&DB Foundation. The other authors declare that they have no competing interests. **Data and materials availability:** All data needed to evaluate the conclusions in the paper are present in the paper or the Supplementary Materials.

Submitted 8 May 2020
Accepted 16 November 2020
Published 16 December 2020
10.1126/scirobotics.abc6878

Citation: T. Kim, S. Lee, T. Hong, G. Shin, T. Kim, Y.-L. Park, Heterogeneous sensing in a multifunctional soft sensor for human-robot interfaces. *Sci Robot.* **5**, eabc6878 (2020).

Science Robotics

Heterogeneous sensing in a multifunctional soft sensor for human-robot interfaces

Taekyoung Kim, Sudong Lee, Taehwa Hong, Gyowook Shin, Taehwan Kim, and Yong-Lae Park

Sci. Robot. **5** (49), eabc6878. DOI: 10.1126/scirobotics.abc6878

Science Robotics (ISSN 2470-9476) is published by the American Association for the Advancement of Science. 1200 New York Avenue NW, Washington, DC 20005. The title *Science Robotics* is a registered trademark of AAAS.